

Analysis of broad-band H α coronagraphic observations

D. Romeuf^{1,4}, N. Meunier², J.-C. Noëns², S. Koutchmy³, R. Jimenez², O. Wurmser⁴,
S. Rochain⁴, and “Observateurs Associés” Team⁴

¹ Centre de Ressources Informatiques, Université Lyon I, 8 avenue Rockefeller, 69373 Lyon Cedex 08, France
e-mail: David.Romeuf@recherche.univ-lyon1.fr

² Laboratoire d’Astrophysique de l’Observatoire Midi-Pyrénées, 57 avenue d’Azereix, BP 826, 65008 Tarbes Cedex, France
e-mail: [noens;meunier]@ast.obs-mip.fr

³ Institut d’Astrophysique de Paris, CNRS and UPMC, 98 bis boulevard Arago, 75014 Paris, France
e-mail: koutchmy@iap.fr

⁴ Observateurs associés/FIDUCIAL, Team of observers at the Pic du Midi coronagraph, <http://www.astrosurf.com/oa>
e-mail: Odile.Wurmser@wanadoo.fr; s.rochain@aliceadsl.fr

Received 6 September 2005 / Accepted 23 September 2006

ABSTRACT

Context. Daily broad-band full-limb H α images of the inner corona were obtained during solar cycle 23 (1994–2005) using the 15 cm Pic-du-Midi coronagraph.

Aims. We want to automatically extract the properties and evolutions of the observed cool HI coronal structures over a wide range of sizes and light fluxes, from small jets and/or spikes to large prominences.

Methods. A tool was developed to process the complete set of stored images. This paper describes the recognition techniques implemented in our software and discusses its use. It includes the removal of the parasitic diffraction ring produced by the set of different occulting disks used throughout the year.

Results. We present and discuss selected results from a statistical analysis of the occurrence of parameters characterizing the observed structures applied to a large sample of observations. It illustrates the capabilities of this software when applied to our database. Strong asymmetries of the activity level over the solar poles become evident, confirming similar results from previous works. We also discuss the distribution of relative light fluxes of these structures over a wide range of sizes.

Conclusions. The complete series of FITS and calibrated images, the list of the detected structures, and their geometric and luminosity evolutions are stored in the BASS2000 solar database catalogue (<http://bass2000.bagn.obs-mip.fr>) and are made publicly available. The H α HI structures observed over the limb of the sun present statistical properties of great interest for understanding its eruptive activity.

Key words. Sun: activity – Sun: corona – Sun: prominences – Sun: coronal mass ejections (CMEs)

1. Introduction

Since 1994, the 15 cm coronagraph at the Pic-du-Midi Observatory (Niot & Noëns 1997), called “HACO” (H Alpha COronagraph), has been used to perform a daily survey of the evolution of the cool structures in the inner corona. Cool coronal structures were episodically studied in the past (Leroy 1972), but no systematic quantitative analysis seems to exist. This is especially true when light fluxes of chromospheric and cool coronal HI structures, as measured over their entire line profiles, are considered.

Our full-limb coronagraphic H α images are being collected using a broad-band filter, with a time cadence that depends on the observed events. This program has provided a database of more than 185 000 images covering the solar cycle XXIII. It was necessary to build special software in order to extract useful information about the HI structures and their time evolutions from this long time series. Tools generally used to treat the full disk images produced by solar telescopes are unfortunately not adapted to processing the full-limb images produced by coronagraphs. The difficulties come essentially from the non uniform distribution of the background intensity in the images produced by the sky brightness and from seeing effects, convolved with the instrumental background, and especially from the bright ring

produced in the inner parts by the occulting system of the coronagraph. The objectives are to permit an automatic treatment of all images obtained by the daily survey. It must produce both series of calibrated images in relative units, corrected from the instrumental and seeing effects, and a list of the positions of the detected structures, in addition to their brightness and geometric properties. It must be able to show the time evolutions of all these parameters and must indicate about the activity in the detected regions at the time of observations.

Automatic recognition techniques have already been applied to H α full disk images taken with narrower pass-bands by Collin & Nesme-Ribes (1995). Recent work has been done on this subject in the context of EGSO¹ by Zharkova et al. (2003). They studied a way to standardize such full narrow pass-band disk images with the purpose of performing some automatic recognition, for filaments in particular (Fuller et al. 2005). To our knowledge the only study aimed at automatically detecting coronal structures (outside the disk) is that of Robbrecht & Berghmans (2004), who propose a technique for recognizing CMEs on LASCO/SOHO images, i.e. much farther from the limb than what is considered here with HACO images. Here we built an automatic recognition software, called SCANPROTU,

¹ European Grid for Solar Observations.

in order to extract all data from the complete set of images provided by the daily survey, such as their behavior, size, luminosity, height, etc. This software includes a calibration procedure of images. All calibrated images, along with the raw data, will be made publicly available in the BASS2000 database in Tarbes–France². The database containing the identified structures will be available in an SQL archive³. A large amount of information will be available on line (such as JPEG files or movies and some properties of the detected structures), while the original FITS files can be requested by all users.

This database enables the comparison of the time evolution of a given structure with other observations at various wavelengths (more particularly those obtained using SOHO instruments such as EIT, SUMER, UVCS, CDS, and LASCO). For example, a small sub-sample has been used by Innes et al. (1999) to perform a multi-wavelength study of a coronal mass ejection, including the dynamical “disparition brusque” (DB) events that play a fundamental role during CMEs. In addition, this database makes it possible to perform a statistical study of the cool structures of the lower corona. As an example of a study that is more extended in time, the initial years of this time series data were used by Noëns & Wurmser (2000), who identified small short-lived polar H α spikes or cool “jets”. They observed a rather strong asymmetry between the North and South Polar Regions and a possible relationship with the polar magnetic field reversal related to the solar cycle. However, considering the amount of data, it is clearly necessary to introduce some more automatic recognition software in order to extract as many structures as possible, using a single identification procedure. It is also important to be able to retrieve as much information as possible from the smallest and finest structures detected with our instrument, such as spikes in addition to large prominences. These fine structures are poorly understood but may take part in the general mass transport of material in the inner corona (Dere et al. 1989; Koutchmy & Loucif 1991; Delannée et al. 1998; Loucif et al. 1998).

The processing described in this paper may also be applied to series of full images produced by other coronagraphs, including space-borne ones (Koutchmy 1987). But it is not suitable for the usual images of the hot corona obtained in emission lines, partly because the structures of this part of the corona are often more diffused and larger in size compared to the dense H α cool structures. In this paper, we describe observations (Sect. 2), the image processing, and the algorithm allowing the detection of the structures (Sects. 3 and 4). Then, in Sect. 5, we present a few new results to illustrate an efficient use of this database to analyze the so-called cool corona. Perspectives are discussed in Sect. 6.

2. Observations

The HACO coronagraph provides full-disk broad-band H α images above the limb, covering a field up to 1.3 solar radius. The occulting disk is changed every month so as to adjust the amount of occultation to the changing apparent size of the solar image due to the yearly motion of the Earth around the sun along its elliptical orbit. Files are written in FITS format, with a set of keywords corresponding to the standards of solar databases like BASS2000, SOHO, and MEDOC. The instrument has evolved

Table 1. Number of observing days, number of images, and average number of images per day for each year from 1994 to 2004.

Year	# days	# images	Av. # images/day
1994	82	4635	56.5
1995	128	8175	63.8
1996	187	9363	50.1
1997	101	6281	62.2
1998	58	3075	53.0
1999	90	8502	94.5
2000	168	13 535	80.6
2001	191	27 170	142.2
2002	162	23 308	139.6
2003	182	31 754	174.5
2004	169	43 979	260.2

over time. Two CCD cameras have been successively used. A 1024 × 1024 Wright CCD 16 bits camera was used from 1994 till 2001. Since 2001, a 2048 × 2048, 14-bit, CCD Apogée AP10 camera is used. With the former camera, the pixel size corresponded to 2.8 arcsec. With the present camera, the pixel size is 1.4 arcsec. The theoretical angular resolution is 1.1 arcsec, although the actual angular resolution is often worse due to the seeing. Several H α filters were successively used in order to optimize the S/N ratio, keeping in mind that the light fluxes we measure should not be too affected by effects due to Doppler shifts of the emission line when dynamical events are picked up. The former filter had a 1 nm *FWHM*. It was used from 1994 to the end of 1995. A second filter with a 0.33 nm *FWHM* was then used during the period 1995–2000. Finally, a third filter with a 0.17 nm *FWHM*, thermally stabilized, was used in the period 2000–2003. Since 2003 a new “improved in quality” (homogeneity, transparency) 0.15 nm *FWHM* filter is used. The software SCANPROTU takes these different parameters into account to provide homogeneous quantitative data.

A team of observers, led by one of the authors (J.-C. Noëns), performs daily observations. The evolution of the capabilities of the coronagraph led to an improvement of the time resolution of the recorded images, see also Table 1. The frames are not taken with a fully automatic procedure: the observers indeed select the optimum rate adapted to the individual evolution of each observed dynamic event in real time, up to 5 images/min when a fast-evolving structure is identified. Only 1 image/min is taken during a period without any dynamical event. In addition, data is obtained for making the flat-field correction and the photometric calibration. For the flat-field measurement, five images are obtained using a white screen illuminated by the sun in front of the entrance objective of the coronagraph. Calibration images are obtained every hour by directly measuring the sun centers intensity through a neutral density placed in front of the objective. Dark currents are automatically corrected for each image. More details about the observations were given by Niot & Noëns (1997). Table 1 shows the number of observing days and the number of images produced annually, as well as the average number of images per day. The rate of observations clearly increased over time so more data was obtained for highly variable phenomena. The gap in the number of observing days in the period 1997–99 is due to a break in scientific activities during the reshaping of the Pic-du-Midi observatory.

3. Flat-fielding and calibrations

Each image is first accurately flat-fielded using a specially designed method. For this purpose, the five flat-field images are

² BASS2000 is a database for groundbased solar observations: http://bass2000.obs-mip.fr/pageac_ang.htm

³ http://bass2000.obs-mip.fr/New2003/Pages/Coro/interro_scanprotu.html

normalized and reduced to a single flat-field image by taking, for each pixel, the median of the values over the five images at that pixel. Then, they are calibrated to remove the diurnal variations in the Earth atmospheric transmission. For this purpose, solar disk images are produced with a calibrated neutral density in order to provide intensities in units of the disk center intensity as measured with a 1 Å wide filter. We also removed effects due to the slow drifts of the narrow interference filters that were successively used. Finally, intensities are expressed in millionths of the solar central intensity of 10^{-5} times its surface, i.e. the luminance of a given pixel is a fraction of $10^{-11} L_s$, with L_s the sun disk center's intensity at this wavelength, over a 1 Å passband and taken over a pixel. The purpose of this unit is to optimize the number of bits used to save the rather large number of images. Sources of uncertainties in this calibration are of two kinds. On a time scale of years, they include the replacements of the H α filters, the filter aging and the effect of dust accumulation inside the instrument. On a time scale of a few hours, they include the variable atmospheric transmission due to the height of the sun in the sky, which is removed during the processing, and to local weather conditions. Our calibration is well-adapted to short term variation, but is more uncertain for long-term variations.

4. The SCANPROTU algorithm

The data is processed one image at a time, but a code is indeed applied to the whole daily time series. After the calibrations described above, the software SCANPROTU is used. It contains the following steps:

- 1. find the disk center and the solar radius in arbitrary units;
- 2. transform into polar coordinates;
- 3. compute the wavelet planes;
- 4. suppress the artefacts and parasitic fringes created by the occulting disk;
- 5. determine an average profile around the limb and filtering processing;
- 6. perform a “pyramidal” analysis;
- 7. compute a calibrated image;
- 8. analyze the properties of each detected structure.

Note that steps 3 to 6 are applied to the polar coordinate images, which are only used to determine the geometry of the structures (position, size). Step 7 is applied to the original image in order to get the intensities associated to each structure.

4.1. Disk center coordinates, radii of the occulting disk, and solar image

The image of the occulting disk is surrounded by a very bright fringe (Fig. 1) of parasitic origin, which is usually slightly asymmetric since the occulting disk and the solar disk do not have precisely the same center. This fringe is due to the light diffracted by the occulting disk. Therefore, the actual radius of the sun does not correspond to the size of this fringe, but is smaller, as illustrated in Fig. 2. For example, simultaneous observations of SOHO/EIT images and HACO images performed on June 14, 1999 (Noëns et al. 2004) have shown that there was a factor of ~ 0.985 between the estimated solar radius and the true solar radius.

First, the position and radius of the occulting disk is determined. Starting from the approximate image center, we search for the first maximum along each radial intensity profile. The center of gravity of the area enclosed inside the inner part of



Fig. 1. Upper panel: raw image after the calibration described in Sect. 3 obtained on August 2, 2000 with the North pole at the top. Lower panel: same image in polar coordinates. The abscissa scale of the lower panel figure covers 360 degrees, and the ordinate scale covers 0.32 solar radius. On both panels the white arrow indicates the location of the bright fringe described in Sect. 4.1 and removed in Sect. 4.4.

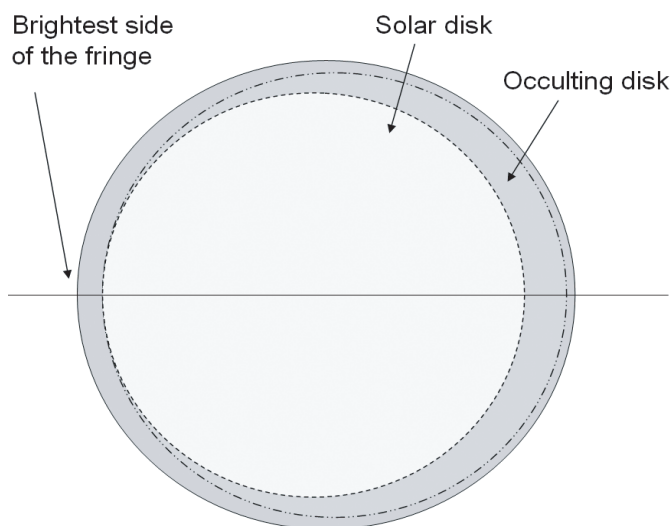


Fig. 2. Schematic to show the various elements to take into account: the occulting disk, the solar disk, the bright parasitic “diffraction” ring due to combined effects inside the instrument and to the seeing.

the bright fringe defined by the positions of these maximum values is used to determine the precise center and the radius of the occulting disk (Fig. 2). Note that the occulting disk may not be perfect and that its effective radius may change in time, due to dilatation and thermal shocks in case of interruption during cloud periods.

The second step is to determine the coordinates of the sun center and its radius. We search for its contour by fitting an

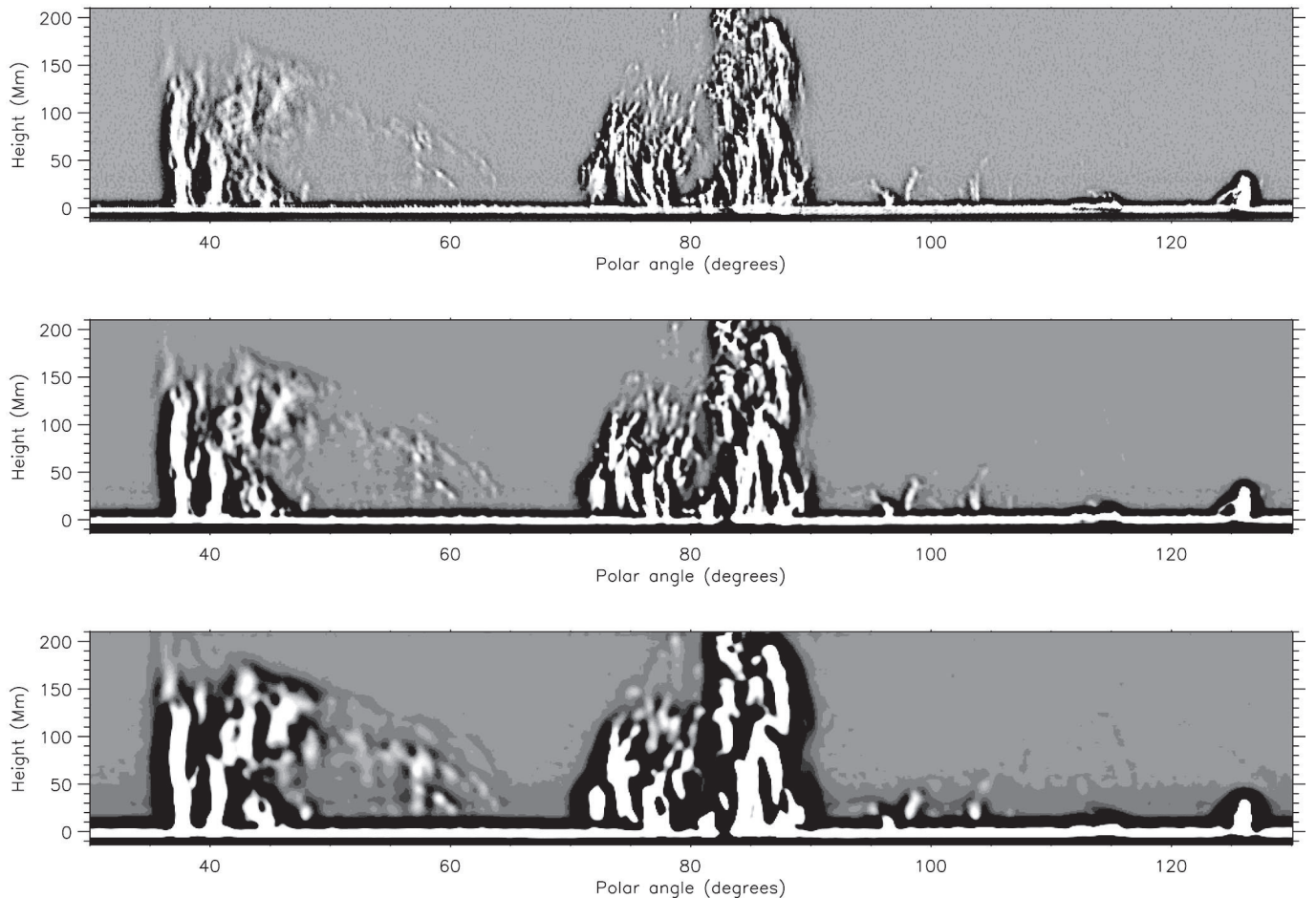


Fig. 3. Example of wavelet planes obtained for a part of the image of Fig. 1. The spatial scale changes by a factor of two between maps. The first map at the top is built with the finest details, including the noise. The last map at the bottom is built with larger structures. The middle map corresponds to intermediate scales. The bright limb fringe is visible on all the maps. Note also the dark artefact at the edges of the structures (Gibbs effect). The height is positive outward the sun.

ellipse using a least-square technique (Fitzgibbon et al. 1999) on the inflexion points along the external part of each radial profile (the inflexion points after the maximum intensity are considered). The parameters of the ellipse are used to define the center and the radius of the solar disk. This method proved to be robust to provide the best image-motion compensation. Normalized and compressed images remapped to 2048×2048 pixels, with the North Pole at the top, are used to create movies with different thresholds available at BASS2000.

4.2. Transformation into polar coordinates

Each image is transformed into polar coordinates. An example is shown at the bottom of Fig. 1. The x -axis represents the polar angle with a resolution of 0.1 degrees. The y -axis represents the distance from disk center, with values from 0.98 to 1.3 solar radius. The first column is centered on the North Pole, the angles being counted counter-clockwise. The algorithm described below to detect and select structures is based on the polar profiles deduced from this polar coordinates field. In the case of the 1024×1024 camera, the typical sun radius is around 400 pixels and 0.1 degrees then represents 0.7 pixels. In the case of the 2048×2048 camera, it represents 1.4 pixels, so there is a slight degradation of the spatial resolution in the second case. However, it is important to keep in mind that the polar coordinate images will be used only to identify structures and never

to determine intensities. Furthermore, because of the seeing, this slight degradation is no concern for determining the geometry of the structures.

4.3. Wavelet plane analysis

Coronagraphic images contain details at various spatial scales (quiescent prominences, eruptive prominences, jets, spikes) from a few Mm to more than 50 Mm. The dynamical range of intensities can reach 4 orders of magnitude. Furthermore, these structures at different scales are often superimposed on each other. Since it is necessary to extract all the structures, even the small ones, a simple threshold on the images could be used, but a specific technique was developed. It was chosen to add to the image those wavelet planes corresponding to the finest details in order to increase the detection capabilities. This step is crucial for determining the positions of the structures. The result is an increased contrast and a better signal-to-noise ratio for fine structures, which will make the determination of the position of the structures more precise. Evidently the resulting image cannot be used for any photometric purpose.

Wavelet planes are computed using the classical “à trou” algorithm (Holschneider & Tchamitchian 1990; Shensa 1992). More details about wavelet techniques were published by Starck & Murtagh (1994). Illustrations of some of the obtained wavelet planes are shown in Fig. 3. The plan corresponding to the

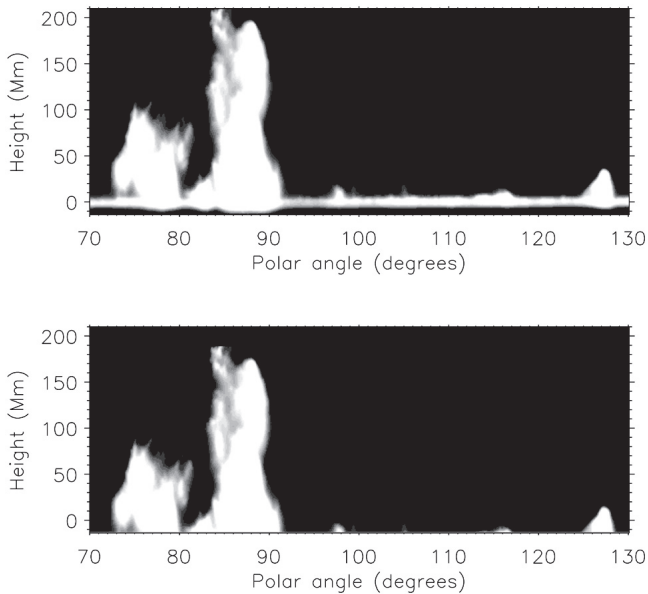


Fig. 4. Illustration of the ring removal processing (see Sect. 4.4) applied to the region shown in Fig. 3. *Upper panel:* image before the correction. *Lower panel:* image after the correction. The height is positive outward the sun.

smallest scale has been chosen to correspond to the finest details seen on our images, which correspond to ~ 2 Mm given the pixel size on the order of 1 Mm. The other plans are such that they sample the different scales up to the largest structures: at each step, the scale is twice the scale of the previous step. The top panel shows the wavelet plane with the finest details, i.e. a few Mm. It illustrates the fact that some of these finest structures are individual structures by themselves (cool “jets”), while other fine structures are included in larger prominences, which will have to be identified using wavelet planes such as those in the lower panel (showing only the large scales). On the other hand, it is obvious that the last wavelet plane would not be suitable for identifying the small jets. This will be discussed in Sects. 4.5 and 4.6. The image used in the next section is a combination of the different wavelet planes with a different weighting.

4.4. Suppression of the parasitic fringe

At this stage the enhanced image still contains the bright fringe described in Sect. 4.1, in addition to the solar structures. The accurate removal of this bright region situated at the bottom of the image is difficult. Several techniques were tested, and the following technique was selected. First, along each radial direction, the signal is convolved with a low-pass filter in order to smooth the profile and make the derivative of the signal less noisy. The fringe location is then defined as the position of the first maximum along the profile (using the first derivative). The center of the Gibbs artefact is determined using a similar technique where structures are not present. Positions where some activity is seen, leading to higher values for the width of the fringe, must be eliminated and replaced by another estimate. Let us call $p(x)$ the position of this minimum for each position x around the sun. The aberrant values in $p(x)$ are eliminated using a median filter, as each value is replaced by the median in p over 40 degrees centered on position x and zeros are added at the top of the position. The choice of the 40 degrees value results from a compromise between the typical size of a prominence on one side (it has to be larger) and the slow variation of the thickness of this

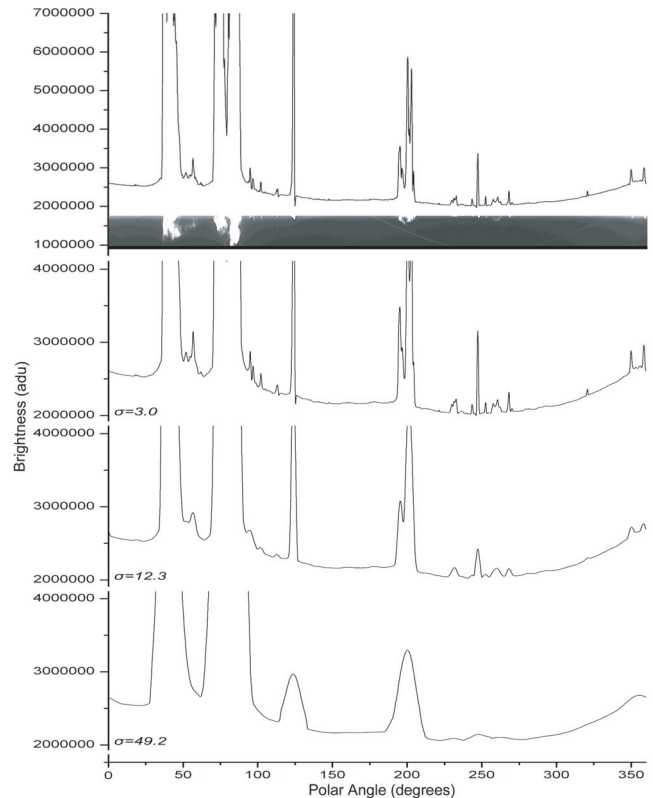


Fig. 5. Example of the scale analysis: profiles versus polar angle for the region selected in Fig. 3. *Top part:* original averaged profiles versus polar angle. The three subsequent rows correspond to profiles convolved with a low-pass filter, increasing the spatial smoothing with a width of 3.0, 12.3 and 49.2 pixels (see Sect. 4.5).

fringe versus the polar angle (see Fig. 2). An example of an image before and after the correction is shown in Fig. 4. We can estimate the typical error on the shift determination to be close to the pixel size, which is small compared to the distortions of the limb shape due to the seeing, for example. The position of the structures should not be significantly affected by this error, which will mostly affect the detection of the smallest structures (a few pixels). This will therefore slightly affect the slopes of the distributions for the small structures (see Sect. 5.1).

4.5. Average profile and scaling analysis

To detect off-limb solar structures, images in polar coordinates are averaged in the radial direction to produce a profile of the averaged brightness versus the polar angle. Note that the background outside actual structures strongly contributes to this average profile. An example is shown in Fig. 5 (upper panel). Its visual inspection shows that all scales are present from small features and spikes (a few Mm) to large quiescent prominences (several 10 Mm). However, small scales can either be present alone or superimposed on a larger-scale structure. The algorithm must therefore be able to separate the structures on various scales. Therefore, we generate a series of profiles where the small-scale structures are increasingly filtered. This is done using a low-pass filter, the original profile being convolved with Gaussian profiles of various widths: 1.5, 3.0, 6.1, 12.3, 24.6, 49.2 pixels are the half-widths at half-maximum (HWHM) of the Gaussian filters. The amplitudes of the Gaussian widths are

chosen to cover the range of scales of the structures we have to identify (see in particular Fig. 3), from small structures (a HWHM of 1.5 pixels corresponds to a width of about 2 Mm) to large structures (49.2 pixels corresponds to a width of about 120 Mm).

An example of the processing is shown in Fig. 5. For each profile, the detection of structures is performed by detecting the profile maximum, derived from the first derivatives, and the location of their inflexion points, derived from the second derivatives. Note that in the case of very large eruption events, we must visually impose the position. This second step is important for studying evolution, such as the total brightness in the case of a large prominence leading to a CME. At this stage, we obtain for each profile 3 values of polar angles determining a structure: the center position and the upper and lower limit positions. A fourth quantity is also computed: we call it the “strength” of the detected structure. It is the sum of the absolute values of the derivative over the entire structure inside the upper and lower limits. This quantity is useful for determining the threshold between background values and actual solar structures. Such a threshold is experimentally defined for each spatial smoothing, as we visually checked on a small data set that we have not eliminated actual structures. Structures whose strengths are below the threshold are eliminated to avoid any false detection. The choice of the threshold has been made in a conservative way, as another algorithm will be applied in Sect. 4.8 to the daily time series in order to eliminate structures that might appear only once.

4.6. Pyramidal analysis

Structures detected on various scales must be analyzed in order to provide a single list of structures. Starting with the largest scale, a pyramidal analysis allows the elimination of the small structures located in a zone where a structure has already been detected at the upper level. More specifically, we first consider the structures defined on the largest scale. This identifies the largest structures, the smallest ones being absent. Then, at the following step (on a smaller scale), two categories of structures are present: those that overlaps an already identified large structure (therefore they are not to be considered) and those not overlapping such structures (they are added to the list of structures). This is repeated until the smallest scale is reached. This is called the “extraction process” or simply the “extraction” further on. A list of positions is derived from this analysis, and it provides the location of the structures described in Sect. 4.8.

4.7. Final products

To produce calibrated images in Cartesian coordinates and to precisely estimate the intensities of the structures, the original images (obtained at the end of Sect. 4.1) are normalized to the same standard. After properly subtracting the background, the data is made available at BASS2000. An example is shown in Fig. 6, where the bright fringe and the background were subtracted. In addition, the average activity level and its standard deviation (showing the temporal variability of the activity level) over a day are computed in order to use this as a selection criterion in database requests. These images are used to extract F_s , the light flux integrated over the whole structure, by summing the intensities of each pixel between the two limits determining the structure (see Sect. 4.8).



Fig. 6. *Upper panel:* the background with the ring computed from the image shown in Fig. 1 (see Sect. 4.7). *Lower panel:* the cleaned image obtained after applying the background plus ring correction.

4.8. Structure parameters

In addition to the positions of each detected structure (lower and upper limits P_1 and P_2 , and central positions P_c), several parameters are computed using the images in polar coordinates, after suppression of the parasitic fringe:

- the height H determined in two steps. First, a fast algorithm provides an estimation by using the radial profile averaged between P_1 and P_2 . Starting from the maximum of the intensity profile, the height where the profile reaches 10% of the maximum intensity gives a first estimate, H_0 . This value is arbitrary in some cases when a prominence is very complex and presents fine structure in the radial direction. A threshold is therefore experimentally defined in order to extract the pixels belonging to the structure. To eliminate possible contamination from the parasitic fringes occurring far from the limb, only pixels below $2H_0$ are considered. The position

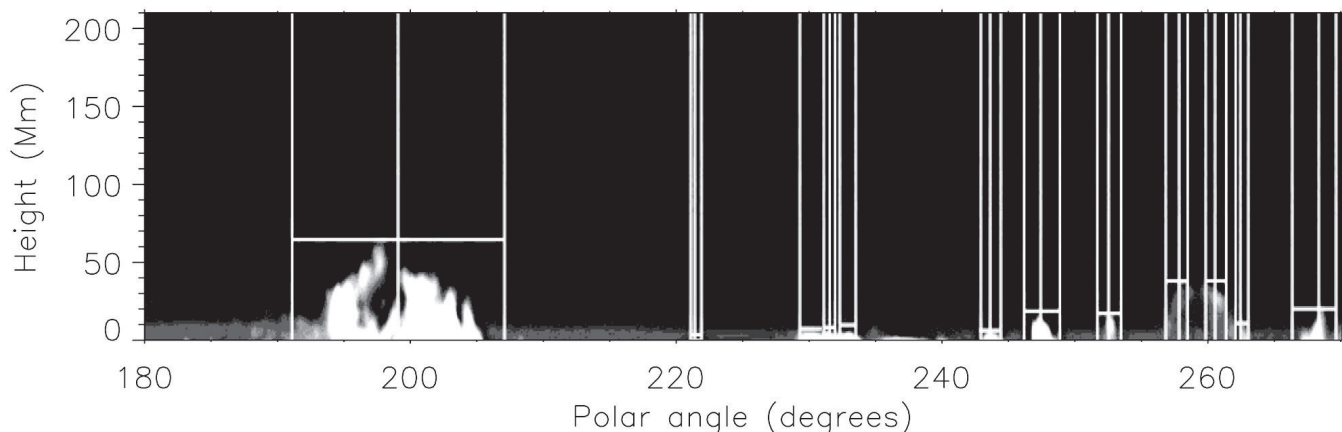


Fig. 7. Illustration to show how the height determination method works for the selected region of Fig. 3. The vertical lines show the limits P_1 and P_2 , as well as the location of the center of the detection P_c of each structure. The horizontal lines show the height H corresponding to each structure.

of the highest pixel defines the new height H , which is expressed in fractions of the solar radius. An example of height determination is illustrated in Fig. 7;

- the effective surfaces in pixel number S_{pix} and in units of 10^{-5} of the solar surface S are estimated using the same experimental threshold, but it is applied to the image where the bright fringe has been removed (see Sect. 4.4). The coordinate transformation is taken into account in this computation;
- the center of gravity of the structure is defined using the same technique as for the effective surface. The coordinates are X in tenth of degrees and Y in pixels.

Note that the position is determined after the convolution described in Sect. 4.5; therefore, these positions slightly overestimate the angular extent of the structures. The set of widths was chosen in order to sample the size ranges of the observed structures as well as possible. Finally, a reliable estimation of the light flux, F_s , is performed on the calibrated image (Sect. 4.7). The intensity is summed between P_1 and P_2 and for heights up to $1.5H$. This represents the light flux in H α with neither the background nor the parasitic fringe.

The errors introduced by the seeing and light conditions are difficult to determine. One possibility is to look at the temporal variation in the integrated flux in a given zone of the image, after removing the long-term variation (daily variation). For low fluxes, the variations are on the order of 5–10% of the flux. The proportion should be much lower for large-flux structures like prominences. However, part of these fluctuations have a solar origin. Furthermore, we do not observe any correlation between the flux variations in various locations along the limb, as could be expected from light variations of instrumental and/or atmospheric origin. This means that the errors on the fluxes due to the seeing and light conditions are quite small, in addition to being random. It is also likely that they affect all structures equally.

Once all detections for a given day are obtained, a filter eliminates structures that are not detected on more than two consecutive images. Additional parameters are obtained by tracking structures from a single image to the next, enabling the study of the evolution of a given structure. It allows the evaluation of a lower limit for the lifetime of the structure, as well as properties such as its maximum height, maximum light flux, or maximum effective surface. Other properties are also computed. This algorithm takes into account that several independent structures can occur at the same location. We call these new

values extracted values. All these characteristics, in addition to other parameters, are stored in a SQL database made available at: http://bass2000.bagn.obs-mip.fr/New2003/Pages/Coro/interro_scanprotu.html. Briefly, the database can be retrieved as follows:

- a simple form can be filled out to provide the requested variables owing to various criteria (date, size, etc.). A large ascii file containing the list of structures and their properties can then be retrieved for subsequent analysis;
- ready-to-use codes are available. They use the database, make simple computations, and provide results mainly as plots such as histograms, plots showing the time evolution of the structure location (coronagram), curves showing the average value of a given parameter versus the polar angle, etc. For a given day, an example of a time sequence of coronagrams is shown in Fig. 8.

5. First results

The software described above was applied to the data set running from 1998 to 2000. During this period covering the last sunspot maximum, the H α filter was stable. Here, we illustrate a few important results in order to show the capabilities of this public database, focusing our attention on the effective surface and light flux distributions, as well as on the apparent relationships between these parameters. Only structures larger than 10 pixels in size were considered in this analysis. This leads to a total of 480 913 individual structures. After the selection described in Sect. 4.8, a data set of 63 711 structures was left. Effective surfaces S were evaluated as a fraction of $10^{-5} S_{\odot}$ (with S_{\odot} the surface of the solar disk) and light fluxes F_s were fraction of $10^{-11} F_{\odot}$ (with F_{\odot} the intensity of the solar disk center in the same spectral band and the same surface defined by the pixel size). As an example, a typical S value of 1 corresponds to a linear size of 3.9 Mm with 100 corresponding to a linear size of 39 Mm.

5.1. Effective surface and light flux distributions

Figure 9 shows the distribution of light fluxes F_s and effective surfaces S for all detected structures. Three regimes can be identified: for effective surfaces i) below 1; ii) between 1 and 10; and iii) above 10, with S expressed as a fraction of $10^{-5} S_{\odot}$.

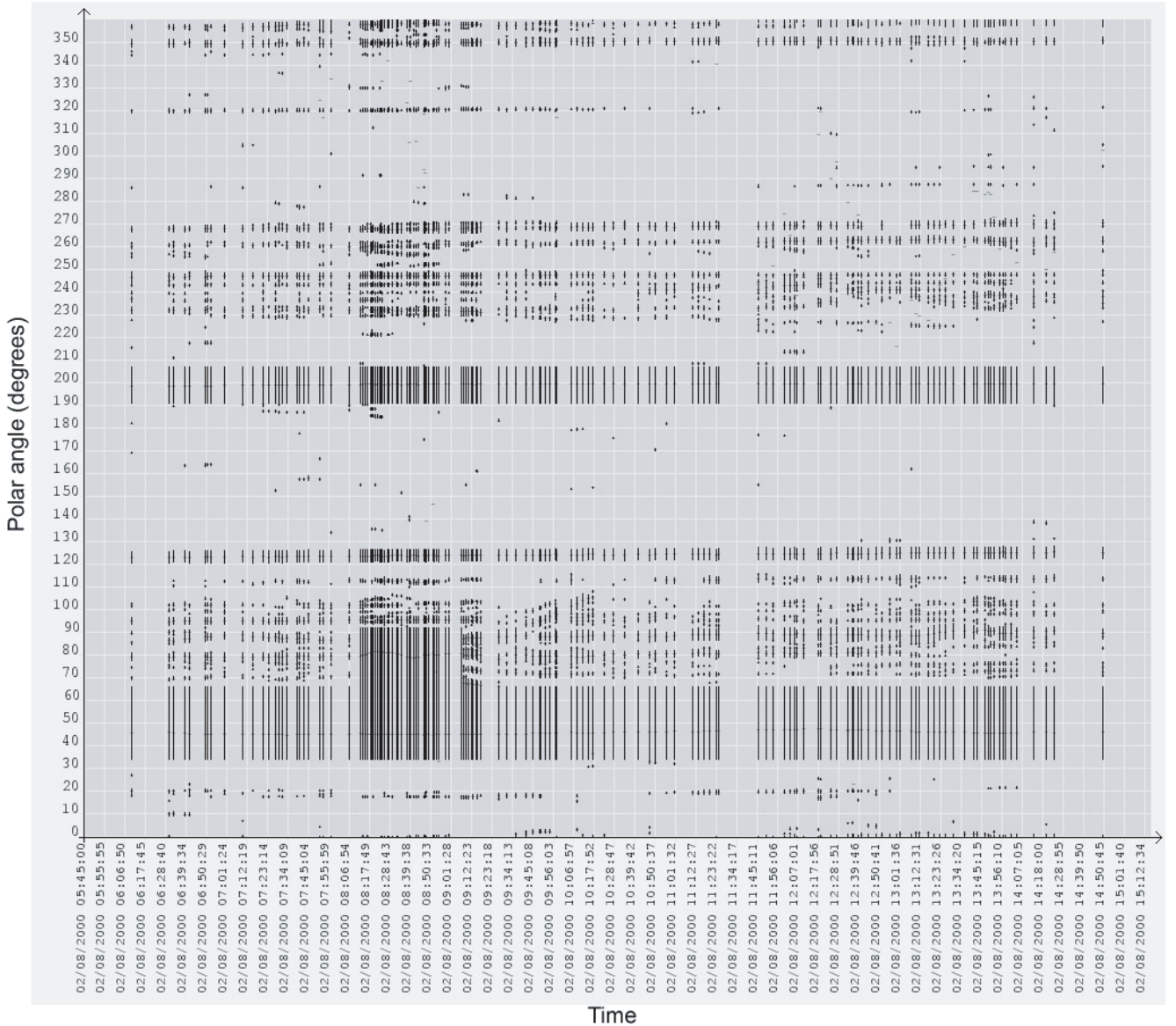


Fig. 8. “Coronagrams” to show the time variations in the location of the detected structures for a continuous typical observing sequence from 6:10 to 14:50 UT, taken on Aug. 2, 2000. The diagram shows all the recorded detections. Solar latitudes are shown along the vertical axis and the time runs along the horizontal axis. The structures are selected using the filtering process described on Sect. 4.8. For this day a “coherence” of the large prominence around the polar angle 48 degrees has been imposed (see Sect. 4.5).

For example, a small cool “jet”, such as those observed in the right part of Fig. 3 (between polar angles 90 and 110°), corresponds to an effective surface S on the order of 10 to 20. Similarly three regimes can be seen in the flux distribution. Distributions are also shown for the values after the “extractions”. In this case, the fluxes and effective surfaces correspond to the maximum value over the day and therefore each structure is counted only once a day.

Different regimes can also be observed there, although they are shifted slightly toward lower values. In the case of the distribution of effective surfaces S after selection (bottom of Fig. 9), we observe a power law for S in the range 0.2–30 and another power law, much steeper, for S larger than ~ 30 , i.e. structures definitely larger than jets. This could be due to the fact that they are related to active regions rather than to the chromospheric network, as is the case for the smallest structures.

5.2. Relationships between structure parameters

Figure 10 shows the relationships between effective surfaces S and fluxes F_s on a log-log scale. The relationship is found to be approximately linear over almost three orders of magnitudes. It corresponds to a power law with a slope of 5/4. For larger structures (i.e. for S larger than ~ 60), the flux is smaller than expected from the linear fit. When looking into more details, there seems in fact to be two regimes in the linear domain, with two distinct slopes below an effective surface of 1 and above it. Below effective surfaces of 1, the slope is 1.108 ± 0.003 for all structures (0.999 ± 0.007 for the maximum values after the “extractions”), and it becomes 1.312 ± 0.001 (1.362 ± 0.007 for the maximum values after the “extractions”) for S larger than 1. The slope is in general larger than 1, showing that in the linear regime, larger structures have a larger flux per square pixel than smaller ones. The exception is for small structures, with a slope consistent with 1, indicating a constant flux per square

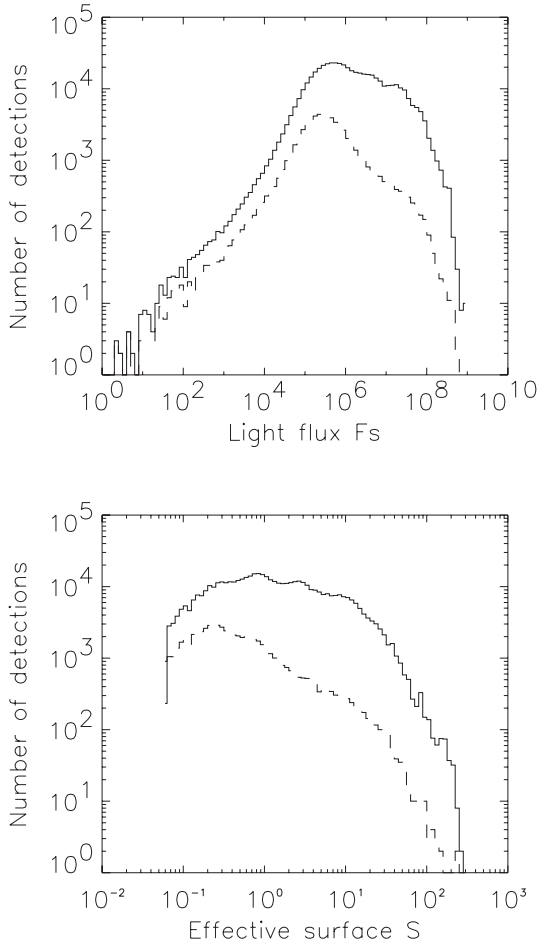


Fig. 9. *Upper panel:* distribution of light fluxes F_s for all structures (solid lines) and the maximum light flux per structure after the selection (dashed line), with F_s expressed as a fraction of $10^{-11} F_\odot$, during the period 1998–2000. *Lower panel:* distribution in effective surface S for all structures (solid lines) and the maximum total light flux per structure after the selection (dashed line), with S expressed as a fraction of $10^{-5} S_\odot$.

pixel for S up to 1. For large structures, the slope is significantly larger after the “extractions”, showing that these parameters are more pronounced when considering only the maximum during the lifetimes of the structures. This suggests different evolutions for the structures depending on their size and a possible influence of the optical thickness on prominence elements. It could also be interesting to look further at the relationship with the level of activity of the analyzed prominences, with their latitudes, etc. We leave this research for a forthcoming paper. Finally, Fig. 10 also shows the variations with size of the rms dispersion of $\text{Log}(F_s)$ in each size bin. It shows that the dispersion is much larger for small structures, as can also be seen on the 2D distribution showing the number of structures versus S and F_s . It is interesting to notice that for small structures, the total extension of F_s values for a given size can reach 4 orders of magnitude, including a long weak tail toward weak light fluxes, which can be seen at the top of Fig. 10.

5.3. Polar angle distribution

Figure 11 shows the distributions versus polar angle for various categories of sizes. The top row shows the distributions for structures identified on all images (i.e. before the selection

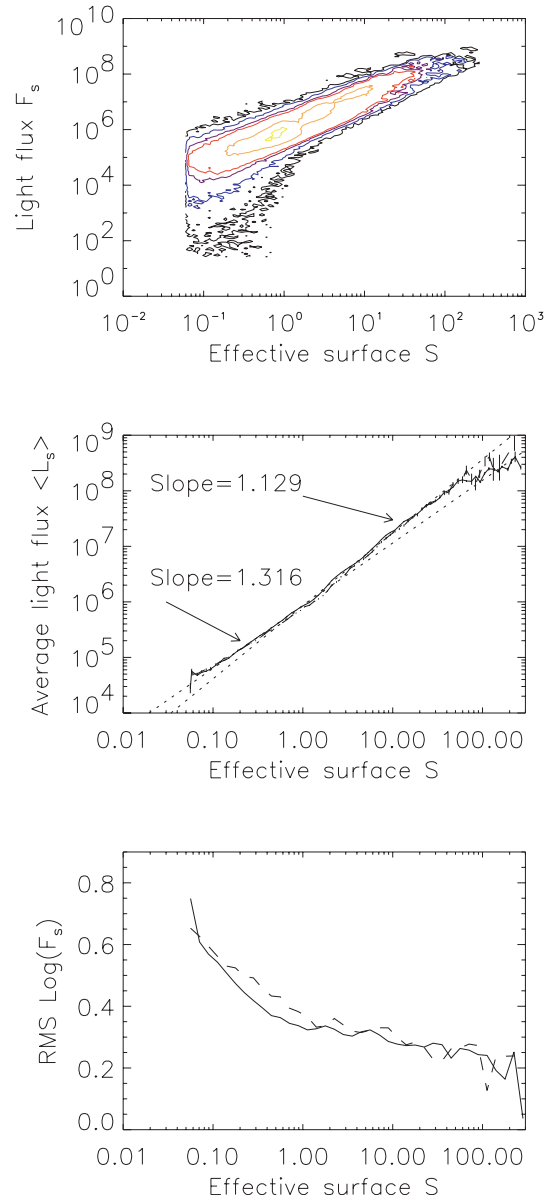


Fig. 10. *Upper panel:* light flux F_s versus effective surface S after the selection (maximum values over the lifetime are used), with S expressed as a fraction of $10^{-5} S_\odot$ and F_s expressed as a fraction of $10^{-11} F_\odot$, for the period 1998–2000. The levels correspond to 1 structure (black), 10 (blue), 50 (purple), 100 (red), 500 (orange), and 800 (yellow). *Middle panel:* light fluxes F_s versus the effective surface S after averaging in boxes of constant size in $\text{Log}(S)$, for all structures (solid line) and after the extraction process (dashed line). The two dotted lines correspond to the linear fits over S in the range 0.1–1 and S larger than 1. *Lower panel:* rms dispersion of $\text{Log}(F_s)$ in each S bin, for all structures (solid line) and after the selection (dashed line).

described in Sect. 4.8). In this case, a given structure is counted as many times as it appears. On the other hand, the distributions in the bottom row correspond to structures after the selection: this eliminates a few uncertain structures and, more important, a given structure is now counted only once per day. The differences between the two approaches is not easy to interpret, but it is in part related to the respective lifetimes of each category of structures. We are concentrating our analysis on the distribution after selection.

Let us first consider the smallest structures, with S smaller than 1. We observe a large number of structures in the activity

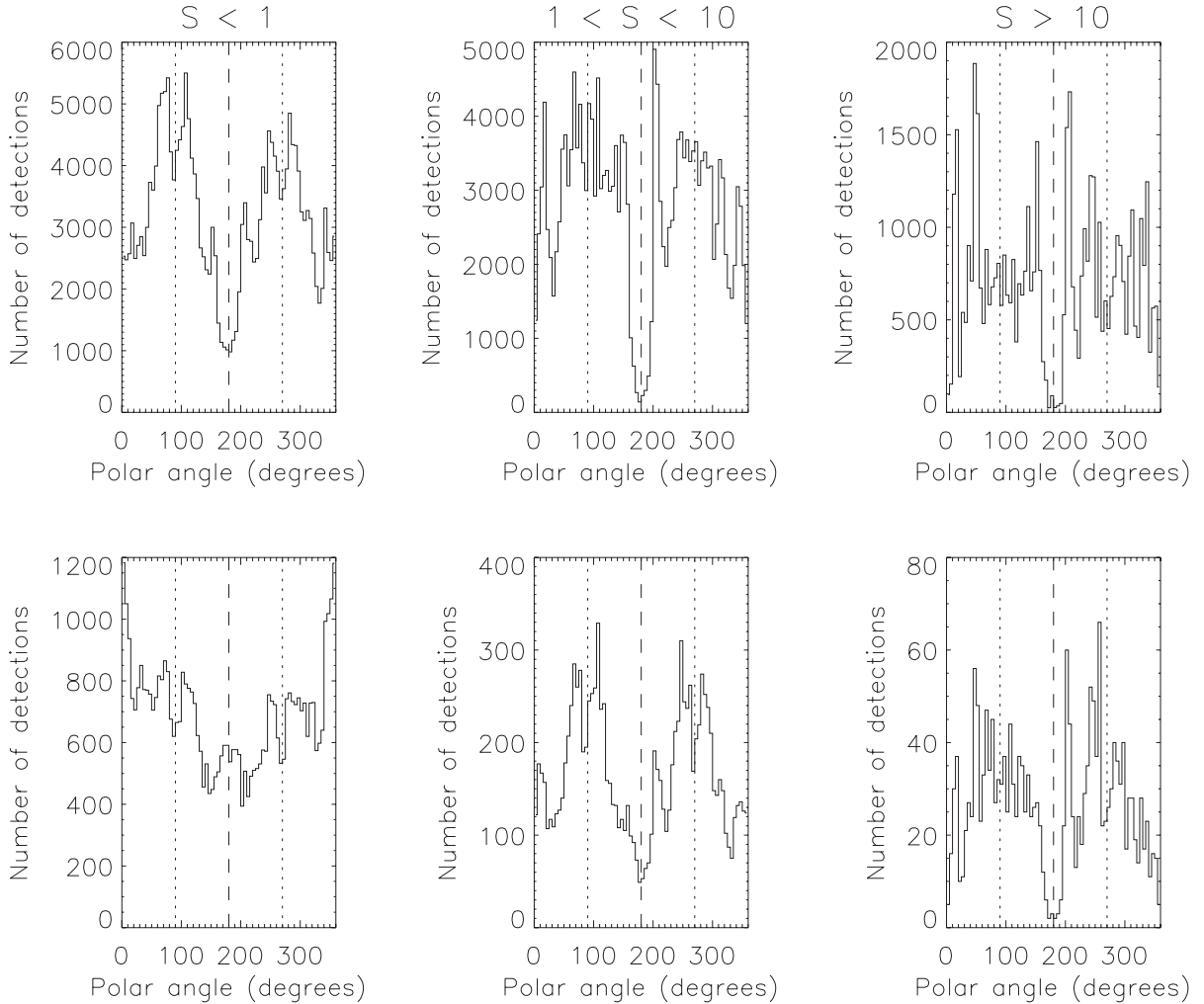


Fig. 11. Distribution of the number of structures versus the polar angle (counted positive counter-clockwise from the North pole), for all structures (*top*) and after the extraction, see 4.8 (*bottom*) over the period 1998–2000, for various size range S : smaller than $1 \times 10^{-5} S_{\odot}$ (*left*), between $1 \times 10^{-5} S_{\odot}$ and $1 \times 10^{-5} S_{\odot}$ (*middle*) and larger than $10 \times 10^{-5} S_{\odot}$ (*right*). The vertical dashed lines represent the solar South pole position, and the dotted lines represent the equator. Note the N-S asymmetry especially strong in polar regions for S smaller than $10 \times 10^{-5} S_{\odot}$.

belts, with a gap at the equator. A smaller gap is observed between the activity belts and the poles, which is much more pronounced in the Northern hemisphere as there is a very strong asymmetry between the two poles (twice as many structures at the Northern pole). The number of structures is also greater close to the poles than at lower latitudes. When considering larger structures, for S in the range 1–10, we observe a similar pattern in the activity belt, with the same gap at the equator. The gap poleward of the activity belts is quite pronounced, again with a definite asymmetry between the numbers of structures at the poles. However, the number of structures is now quite small, as the distribution is dominated by the activity belts. Large structures (S larger than 10) follow a pattern close to the structures in the 1–10 S range. In particular, they also show strong peaks in the 70–80° latitude range (especially in the Southern hemisphere), in addition to the activity belts and strong gaps at the poles. However, the distributions show a larger dispersion.

The dominating features for all structures are therefore small gaps in activity at the equator and just above the activity belt, as well as a strong asymmetry between hemispheres, especially close to the poles. Very small features are definitely more present at the poles, and they have their highest rate of occurrence there.

The gap at intermediate latitudes could be related to the fact that it has been difficult to establish a connection between the high latitude branch of solar activity (observed in the corona and using filaments as tracers) and the low latitude one (activity belt), as illustrated for example in Leroy & Noëns (1983). This is of particular interest to the solar dynamo theories as it provides some constraints on the behavior of the dynamo waves. The North-South asymmetry may also be related to the dynamo action. The fact that it is more pronounced at high latitudes shows that the different components of the solar cycle (here the low-latitude branch and the high-latitude one) do not behave in the same way. We cannot go further because the data considered in this paper cover just a part of the solar cycle. It is our objective to study the evolution of the North-South asymmetry of the distribution of small structures during the whole solar cycle and its possible relationship with the polar magnetic field reversal in a forthcoming paper.

6. Conclusion

Special software was developed to process the large data set of coronagraphic data collected since 1994 in daily surveys at the Pic du Midi Observatory. This software allows the detection of structures over a wide range of sizes, from small spikes to large

prominences. The preliminary results indicate interesting properties over this wide range of light fluxes, i.e. over almost eight orders of magnitude and over more than three orders of magnitude in effective surfaces.

The distributions of fluxes and effective surfaces show three different regimes. The variations in fluxes with structure size is close to linear over three orders of magnitude, with two slightly different slopes for structures below or above 1 (this threshold corresponds to a linear size of 3.9 Mm). The large amount of samples also allows the study of the latitude distribution for the different categories of set and shows a well-structured organization, as well as asymmetries between hemispheres, as already observed by Noëns & Wurmser (2000). This database can therefore potentially be used to study the parameters of small-scale structures in detail, such as their spatial distribution in latitude, their lifetime distribution, as well as the variation in their properties over the solar activity cycle and the relationship with the closest active regions, eruptions, etc., taking the difference between the Northern and Southern hemisphere distributions into account. In this context, we recall that prominences have disk-filament counterparts and, accordingly, they are good proxies of magnetic neutral sheets well inside the inner corona. This will be the subject of future work.

The statistical study of large structures such as prominences is then made possible, as it will be easy to follow their variations in brightness and height, including those leading to CMEs. In addition, these observations can easily be used in comparison to other data, such as that obtained by EIT and SUMER on SOHO in EUV and by LASCO at a much higher altitude above the limb. Finally, the tool developed in this work could be applied to any other coronagraphic data in H α and partly to other coronagraphic data, including those obtained with externally occulted instruments in space (see Koutchmy 1988). It will, of course, be extensively used to process the data from the new coronagraphic and chromospheric instruments currently being developed for the corona at the Pic du Midi Observatory.

Acknowledgements. Living expenses of the large number of associated observers (O.A.) and most of the new equipment were covered by FIDUCIAL. Observations are also supported by PNST of the CNRS and INSU, Observatoire Midi-Pyrénées, Laboratoire d'Astrophysique of OMP and Institut d'Astrophysique de Paris, CNRS, and UPMC. We thank the BASS2000 technical staff, as well as the technical teams of the Pic du Midi Observatory, for their help. We thank C. Latouche for his permanent interest and confidence, G. Stellmacher for reviewing the manuscript, Th. Roudier for useful discussions, J.-M. Abbadie for help running Pic du Midi facilities for us, J.-C. Vial for his interest and the anonymous referee for meaningful suggestions that led to substantial improvements in the paper.

References

- Collin, B., & Nesme-Ribes, E. 1995, *C. R. Acad. Sci. Paris*, 321(IIb), 77
 Delannée, C., Koutchmy, S., Delaboudinière, J.-P., et al. 1998, in *Solar jets and coronal plumes*, ESA SP-421, 129
 Dere, K. P., Bartoe, J. F., Brueckner, G. E., & Recely, F. 1989, *ApJ*, 95, L345
 Fitzgibbon A., Pilu, M., & Fisher, R. B. 1999, *IEEE Transactions on pattern analysis and machine intelligence*, 21(5), 476
 Fuller, N., Aboudarham, J., & Bentley, R. D., 2005, *Sol. Phys.*, 227, 61
 Innes, D. E., Inhester, B., Srivastava, N., et al. 1999, *Sol. Phys.*, 186, 337
 Koutchmy, S. 1988, *Space Sci. Rev.*, 47, 95
 Koutchmy, S., & Loucif, M. L. 1991, in *Mechanism of chromospheric and coronal heating*, Heidelberg Conf., ed. Ulmschneider, et al., 152
 Leroy, J.-L. 1972, *Sol. Phys.*, 25, 413
 Leroy, J.-L., & Noëns, J.-C. 1983, *A&A*, L1
 Loucif, M. L., Koutchmy, S., Stellmacher, G., et al. 1998, in *Solar jets and coronal plumes*, ESA SP-421, 299
 Niot, J. M., & Noëns, J.-C. 1997, *Sol. Phys.*, 173, 53
 Noëns, J.-C., & Wurmser, O. 2000, *Ap&SS*, 273, 17
 Noëns, J.-C., Balestat, M.-F., Jimenez, R., et al. 2004, in *Multi-Wavelength Investigations of Solar Activity*, Saint-Petersburg 14-19 June 2004, (Cambridge University Press), IAU Symposium, 223, 291
 Holschneider, M., & Tchamitchian, P. 1990, *Les ondelettes en 1989*, ed. P.G. Lemarié, (Springer Verlag), 102
 Robbrecht, E., & Berghmans, D. 2004, *A&A*, 425, 1097
 Romeuf, D., Rochain, S., Jimenez, R., et al. 2004, *Atelier PNST*, 26–29 Jan. 2004, Autrans, Livre des résumés, 109
 Shensa, J. 1992, *IEEE. Trans. Signal Process.*, 40(10), 2464
 Starck, J.-L., & Murtagh, F. 1994, *A&A*, 288, 342
 Zharkova, V. V., Ipson, S. S., Zharkov, S. I., et al. 2003, *Sol. Phys.*, 214, 89